Manuscript Details

Manuscript number IE_2016_393

Title Fragmentation of an Advanced Ceramic under Ballistic Impact: Mechanisms and Microstructure

Article type Research Paper

Abstract

In this paper, the impact-induced fragmentation of a commercially available hot-pressed boron carbide is explored. Fragmentation has been noted previously by many authors to be important in the impact performance of advanced ceramics, and so this paper seeks to provide some of the first near-complete and detailed measurements of individual fragment size and shape distributions available in the literature. Fragment size and shapes are quantified using methods developed in previous papers by the authors, and results reveal that two distinct fragmentation mechanisms exist as a consequence of the impact failure of boron carbide: one mechanism that creates small fragments that is associated with the coalescence of fractures originating from carbonaceous defects in the material, and one that creates larger fragments that is associated with structural failure (e.g., radial and circumferential cracking). While these mechanisms are similar to those noted for uniaxial compressive failure, results presented here highlight the importance of fragment shape as a consequence of impact failure. Namely, results indicate that both blocky and shard fragments are formed during impact into a boron carbide plate. Fragment types span across both the small and large fragmentation mechanisms. Using Scanning Electron Microscopy, blocky fragments were found to be associated with the predominant growth of cracks parallel to the impact direction, while shard fragments contain fracture surfaces that are associated with crack growth and coalescence in a direction perpendicular to the impact direction. This is believed to be a consequence of structural bending. No amorphous features were found on any fragments observed in this study (determined using Raman Spectroscopy), suggesting brittle fracture may be the dominant mechanisms that creates the shard fragments. Altogether, the implications of these results is that one can control fragment size and shape by controlling the carbonaceous defects population in boron carbide.

Keywords impact fragmentation; brittle failure; advanced ceramics; boron carbide; defects

Corresponding Author James Hogan

Corresponding Author's Institution University of Alberta

Order of Authors James Hogan, Lukasz Farbaniec, Debjoy Mallick, Vladislav Domnich, Kanak Kuwelkar, Tomoko Sano, James W. McCauley, K.T. Ramesh

Submission Files Included in this PDF

File Name [File Type]

IE_2016_393 Review Response_Second_Response.pdf [Response to Reviewers]

Hogan_IJIE Revision.pdf [Manuscript File]

IJIE Submission Highlights.docx [Highlights]

Submission Files Not Included in this PDF

File Name [File Type]

BC_Ballistic_Frag_v2_no_model_IJIE Revision.tex [LaTeX Source File]

Hogan_BC_bib.bib [LaTeX Source File]

Tile_Microv1.eps [Figure]

ballisticfrag_scatter.eps [Figure]

size_AR.eps [Figure]

failuremechanismsballistic.eps [Figure]

RamanXRDv2.eps [Figure]

defect_fragmentsizes.eps [Figure]

tomoko_ballistic.eps [Figure]

To view all the submission files, including those not included in the PDF, click on the manuscript title on your EVISE Homepage, then click 'Download zip file'.

Dear Dr. Charles Anderson Jr.,

I enclose a second revised manuscript for our study titled “Fragmentation of an Advanced Ceramic under Ballistic Impact: Mechanisms and Microstructure” for publication in the *International Journal of Impact Engineering*. A response to the reviewer is provided that outlines key contributions and publication merit without the inclusion of more experiments, which we believe would be outside of the intended scope of our study. We hope that the Journal and reviewer are satisfied with the response, and the Journal takes into consideration the previous statement by the reviewer (“*That said, I have no problem if the Journal elects to publish the manuscript*”) and elects to publish the article.

Sincerely,

Jamie Hogan

Specific Comments from the Reviewers

Reviewer 1

This reviewer's opinion, concisely stated, is that publication of the subject work is premature.

The manuscript describes an observation on a single material that fragment size and aspect ratio correlate with defect size and spacing.

The time to publish is when the authors have results on a second material having a different defect microstructure and can evaluate their hypothesis. The authors say they are undertaking that task.

An alternative justification for publishing is to use the current results to explore the ability of Hogan's fragmentation model to link microstructure, mechanical properties, and average compressive fragmentation size.

The current state of the manuscript seems to this reviewer to be a report on progress, rather than an archive-able technical publication. *That said, I have no problem if the Journal elects to publish the manuscript.*

Response: We thank the reviewer again for his/her review. It is clear that we did not do a sufficiently good job of explaining how the two materials considered in the paper relate to the issues that the paper addresses. This second revision clarifies that point and addresses the concern of the reviewer.

This manuscript examines TWO materials. The first is the hot-pressed boron carbide, on which we describe the microstructure and the fragmentation results in detail. From these results, we draw the hypothesis that the reviewer notes. In the discussion, a second material is considered: the tape-cast pressureless sintered boron carbide material studied by Sano et al. This is a completely different material, with an entirely different defect microstructure, and we compare the impact performance of the two materials. The tape-cast material examined by Sano et al, was first studied by Paliwal, Sano, Chin, McCauley and Ramesh under high-strain-rate loading, the results of which were presented at the Cocoa Beach meetings of the American Ceramic Society but never published. Sano et al. then performed ballistic evaluations of that material and the Coortek material, which we draw upon for comparison in this paper. The distinction between the two materials that we discuss in the manuscript is both subtle and important. They are both boron carbide; however, the two processing routes are very different (hot-pressing versus tape casting) and they are made by two different companies (Coorstek and Toto). A consequence of this is that the local stoichiometry and grain size distribution are different, in addition to the change in the distribution of carbonaceous inclusions (which come for the sintering additives). Thus, although the defect distributions in the two materials are very different, and we show that this has an effect on the failure processes, and the impact performance. We believe the performance is affected by microstructure as a consequence of microstructural effects on fragmentation based on early paper results. We note though, it is not possible to say that the carbonaceous defects and fragmentation are exclusively responsible in the Sano et al. case. It is the case, however, that a comparison with the level of fidelity that we have performed with respect to microstructure has never been made before, and therefore we believe this represents a valuable contribution to the literature.

Finally, a gentle note regarding the study of an additional material with tailored microstructure: the reviewer is perhaps not aware that the cost of generating a fully controlled second hot-pressed material with a new controlled defect distribution is very high. The manufacturing procedures used for these advanced ceramics are the primary competitive advantage of these materials producers. We do not believe it is financially feasible to perform such a comparison within a University setting.

Finally, our results demonstrate some of the first links between failure and the carbonaceous defects, as well as provide some of the most complete set of impact fragmentation measurements in the literature. Combined, these results provide some guidance to manufacturers as well as a valuable data set to modelers. We believe these represent a valuable contribution to the literature, and thus hope that the paper is accepted for publication.

Fragmentation of an Advanced Ceramic under Ballistic Impact: Mechanisms and Microstructure

James David Hogan[a,b], Lukasz Farbaniec[b,c], Debjoy Mallick[b,d], Vladislav Domnich[e], Kanak Kuwelkar[e], Tomoko Sano[d], James W. McCauley[b,d], Kaliat T. Ramesh[b,f]

[a]*Department of Mechanical Engineering, The University of Alberta, Edmonton, AB T6G 2R3, Canada*
[b]*Hopkins Extreme Materials Institute, The Johns Hopkins University, Baltimore, MD 21218, USA*
[c]*Institute of Shock Physics, Imperial College of London, London, SW7 2AZ, UK*
[d]*Weapons and Materials Research Directorate, U.S. Army Research Laboratory, Aberdeen Proving Ground, MD 21005*
[e]*Department of Material Science and Engineering Rutgers University, Rutgers University, Piscataway, NJ 08854*
[f]*Department of Mechanical Engineering, The Johns Hopkins University, Baltimore, MD 21218, USA*

Abstract

In this paper, the impact-induced fragmentation of a commercially available hot-pressed boron carbide is explored. Fragmentation has been noted previously by many authors to be important in the impact performance of advanced ceramics, and so this paper seeks to provide some of the first near-complete and detailed measurements of individual fragment size and shape distributions available in the literature. Fragment size and shapes are quantified using methods developed in previous papers by the authors, and results reveal that two distinct fragmentation mechanisms exist as a consequence of the impact failure of boron carbide: one mechanism that creates small fragments that is associated with the coalescence of fractures originating from carbonaceous defects in the material, and one that creates larger fragments that is associated with structural failure (e.g., radial and circumferential cracking). While these mechanisms are similar to those noted for uniaxial compressive failure, results presented here highlight the im-

---

Email address: `jdhogan@uablerta.ca` (James David Hogan)

portance of fragment shape as a consequence of impact failure. Namely, results indicate that both blocky and shard fragments are formed during impact into a boron carbide plate. Blocky and shard fragment types span across both the small and large fragmentation mechanisms. Using Scanning Electron Microscopy, blocky fragments were found to be associated with the predominant growth of cracks parallel to the impact direction, while shard fragments contain fracture surfaces that are associated with crack growth and coalescence in a direction perpendicular to the impact direction. The shards are, thus, believed to be a consequence of structural bending. No amorphous features were found on any blocky or shard fragments observed in this study (determined using Raman Spectroscopy), suggesting brittle fracture may be the dominant mechanisms that creates the shard fragments. Altogether, the implications of these results is that one can control fragment size and shape by controlling the carbonaceous defects population in boron carbide. This should help in the design of next-generation advanced ceramics for personal protection.

Keywords: impact fragmentation; brittle failure; advanced ceramics; boron carbide; defects

1. Introduction

The impact of a projectile into a target results in the activation of spatially and temporally evolving failure mechanisms originating from defects, including plasticity, phase transformations, and fracture. These mechanisms eventually manifest in fragmentation sizes, shapes, numbers and ejection velocities. The effects of fragmentation on the ballistic performance (resistance to penetration) of monolithic systems has been investigated by Krell and Strassburger [1], who noted that certain fragment size and shape can lead to better erosion of the projectile and energy dissipation. This has also been noted previously by, for example, Woodward et al. [2]. Other investigations involving the impact fragmentation of ceramics [3–5] have focused on studying the effect of material properties on performance. Krell and Strassburger [1] also discuss the links between performance and properties, and recognized that often both positive and negative correlations have been reported between performance and material properties such as strength, stiffness, and fracture toughness. The ambiguity of the results renders the design of ceramics quite challenging. Not often considered is the effect of microstructure on performance, with few studies performing detailed characterization on materials that are under investigation. In this study we build on these concepts as we attempt to link material properties and the microstructure with the impact fragmentation of a well-characterized hot-pressed boron carbide.

Boron carbide has received considerable attention in the literature as a suitable lightweight armour ceramic because of its high hardness and relatively low density in comparison to other advanced ceramics [3–6]. Boron carbide, however, has been shown to have an interesting impact response, in that: (1) the fragmentation behavior has been observed to change beyond 850 m/s [7], (2) the velocity of the damage wave has been shown to be constant before 650 m/s, after which it steadily increases [3], and (3) it has been observed to have no mescall zone [5]. Note that different projectiles, target geometry, levels of confinement, and materials were used across these and many experiments involving boron carbide. None-the-less, they provide some guidance into the impact behavior of the material. For example, Transmission Electron Microscope analysis of the fragments from Moynihan et al. [7] by authors Chen et al. [6] revealed that the change in fragmentation may be related to the onset of a phase transformation, termed “amorphization”. Amorphization has also been reported to be associated with a decrease in impact performance, and since then, amorphization of boron carbide has received a considerable amount of attention in the literature [8–13].

In this paper, the impact fragmentation of boron carbide is studied for impact velocities of 275 and 930 m/s. These impact velocities are motivated by the interesting impact behavior previously described, where we seek to observe any transitional behavior in this material. In previous papers by the authors, the focus was on strength [14] and fragmentation [15] of the same hot-pressed boron carbide in uniaxial compression. In those papers, two fragmentation mechanisms were noted as a result of uniaxial compressive failure: one mechanism associated with the coalescence of fractures between carbonaceous defects, and one mechanism associated with structural failure. Using insights from those studies and new results involving silicon carbide, the authors developed a compressive brittle fragmentation model framework [16] that showed reasonable agreement with experimental measurements of compressive brittle fragmentation. In this current paper, this past work is expanded on by exploring the fragmentation mechanisms associated with impact of a spherical projectile into a styrofoam-confined boron carbide tile; noting the stress-state and strain-rates are more varied and complicated during impact than uniaxial compression. Impact-induced fragmentation processes have been widely noted in the literature to be important in ballistic performance [1, 2, 7, 17, 18], and so this paper seeks to use previous methods developed by the authors to provide some of the first near-complete distributions of individual fragment size and shapes in the literature. A similar framework for studying fragmentation is followed as presented in [15, 16], but expanded for greater consideration for fragment shape. Shape consideration is motivated by Moynihan et al. [7], who noted a drastic increase in high-aspect-ratio ”shard” fragments beyond a critical impact velocity of 850 m/s. In this paper, measurements of fragment size and shapes are used to inform about impact failure processes that are assessed through analysis of the failure surfaces using Scanning Electron

Microscopy (SEM) and Raman Spectroscopy mapping. Key defects contributing to failure and fragmentation are identified in the microstructure, and then the spacing between these key defects are linked with fragmentation measurements. Finally, the experimental observations are discussed in the context of previously performed impact experiments by Sano et al. [19] on two boron carbide materials with different defect microstructures, with the objective of making links between microstructure, fragmentation, and impact performance.

2. Experimental Setup

The impact experiments were conducted at the U.S. Army Research Laboratory, Aberdeen Proving Ground, MD, USA. A 6.35 mm diameter spherical projectile made of 93 % tungsten carbide, 6 % cobalt, and 1 % nickel was impacted at velocities of 275 m/s and 930 m/s (measured using flash x-ray) into targets that were 55 mm x 70 mm and 8 mm thick. The targets were made of a hot-pressed boron carbide (Coorstek, Inc.) with a Young's modulus of 430 GPa and a density of 2,510 kg/m^3. The material was received as plates, with the thickness direction of the plate parallel to the hot-pressing direction termed "through-thickness" (TT), and the two principal directions perpendicular to this termed "in-plane" (IP). The plate is conceptualized in the schematic in Figure 1. Blue boxes denote optical or SEM images that are captured of TT surfaces, and red boxes for the imaging of sample orientations of the IP surface. Shown in Figure 1a and b are optical micrographs of both planes. All optical microscope images were taken using a Zeiss optical microscope with an AxioCam MRC camera. Three different microstructure features are labelled in the two micrographs: (1) larger carbonaceous inclusions that are circular in TT and elliptical in IP (highlighted with black circles in both images). These inclusions are disk-like in three dimensions with a preferred orientation that is normal to the hot-pressing direction (as conceptualized in the top left schematic). (2) smaller spherical features that are primarily carbonaceous in composition, although sometimes they are pores (highlighted with red circle). (3) brighter ceramic phases that have been identified as aluminium nitride and boron nitride (blue circle). A detailed description of the microstructure is described in Hogan et al. [14, 15], and Farbaniec et al. [20]. In Figure 1, the impact direction is parallel to the hot-pressing direction; and this is also denoted. The impact direction is into the page in Figure 1a and down into the microstructure in Figure 1b.

Targets were mounted inside an acrylic box that was 200 mm long in the direction of impact, 460 mm in height, and 460 mm wide. The box walls were 10 mm thick and lined with 38 mm thick ballistic gel. The gel captures some of the fragments, while the remainder are collected inside the box during the experiment. With this setup, greater than 90 % of the original target mass was recovered, and we believe that these measurements represent some of the most complete set of impact fragmentation results in the literature. Post-experiment, a Zeiss optical microscope with an AxioCam MRC camera was used to image fragments, and image processing techniques developed in Hogan et al. [15] were used to determine fragment size (longest spanning dimension) and aspect ratio (defined in Figure 3c). A TESCAN MIRA3 field emission Scanning Electron Microscope (SEM) with Energy Dispersive Spectroscopy (EDS) capabilities was used to image failure surfaces and to identify failure mechanisms.

Lastly, a Renishaw InVia Raman microspectrometer equipped with a 633 nm laser and a 50x objective lens was used for Raman analysis of fracture surfaces. Particular attention was given to the existence of amorphous features on the shard fragments, as alluded to in the Moynihan et al. [7] and Chen et al. [6] studies. We acknowledge that some amorphization features may still exist on some of the smallest fragments not collected in this study, or those that were not investigated using Raman (we looked at tens of fragments). The spatial dimensions of the analyzed volume at each position of the laser probe were ≈2 μm laterally and ≈1 μm axially. Raman measurements were done at ambient conditions. For Raman imaging, sets of Raman spectra were collected over the selected areas with a 1 μm step size. Peak deconvolution was performed using the Renishaw Wire 3.2 software and Raman maps created based on the intensity of the peaks corresponding to the phase of interest.

3. Experimental Results

In the results section, the fragment size and shape measurements from the impact experiments are explored. SEM and Raman Spectroscopy are used to identify key defects that contribute to failure. Once identified, the inherent microstructural spacing between these key defects are linked to fragment size and shape measurements.

3.1. Fragment Characterization: Sizes and Shapes

Initially, an optical microscope image of some ballistic fragments from the 930 m/s impact experiment is presented in Figure 2a. Two types of fragment shapes are observed: (1) elongated fragments that have higher aspect ratios, and (2) blocky fragments with aspect ratios closer to 1. The aspect ratios and fragment size computed using imagine processing of over 700 images are shown in the scatter plot in Figure 2b. The fragment size is taken as the major axis dimension (longest spanning dimension), while the aspect ratio is defined as the ratio between the major and minor axes. Interestingly, two distinct groups of fragments are observed in Figure 2b: (1) fragment sizes less than 30 μm in size and (2) greater than 70 μm. Work by Hogan et al. [15] has shown that these fragmentation length scales are associated with defect spacings of the graphitic disk defects in the microstructure, which will be discussed later. Comparable results exist for 275 m/s case.

Now that interesting characteristics of the fragment shapes and sizes have been identified, the effect of impact velocity on fragmentation results is examined in Figure 3, where a plot of the cumulative distribution of aspect ratio and fragment size for both impact velocities is shown. The cumulative distribution is defined in [15] and is given as:

$$G(x) = \int_0^x g(\bar{x}) d\bar{x} \tag{1}$$

where $g(\bar{x})$ is the probability distribution of fragment sizes. The fragment size data set is a discrete set of n fragments with sizes of ℓ_i (i=1...n). Ordering this data for increasing fragment size, and assigning a probability of $1/n$ to each fragment, the normalized empirical cumulative distribution function, or eCDF, can be computed as the sum of these probabilities:

$$G_e(\ell) = \frac{1}{n} \sum\nolimits_{i=1}^{n} I(\ell_i \leq \ell) \tag{2}$$

where the indicator function I has a value of 1 if $\ell_i \leq \ell$ and 0 otherwise. In addition to the normalized distribution, the non-normalized eCDF can also be computed. This is done to reveal additional trends not observed in the normalized distributions.

Initially the normalized eCDF of the fragment sizes is considered in Figure 3a, where the 275 m/s velocity experiment is plotted using the blue line and the 930 m/s velocity experiment is plotted using the green line. For the lower velocity case, there are few fragments less than 70 μm and these represent less than 1 % of the total fragment population. For the higher velocity case, the curve shifts to the left, with the exception of fragments larger 1,300 μm, indicating that the fragments are relatively smaller for the higher velocity case. This shift is expected and is a result of (1) additional cracking needed to dissipate the additional strain energy for the higher impact velocity, and (2) the activation of more defects due to the increased loading rate, and subsequent coalescence of cracks originating from these defects. Also observed for the higher velocity case is an increase in the fragment population below 30 μm, as well as inflections at 30 μm and 70 μm, reflecting the behavior observed in the scatter plot. These fragment sizes are believed to be related to the inherent microstructural defect spacing length scales.

The non-normalized cumulative distribution of fragment sizes is shown in Figure 3b. The average fragment size with standard error for the 275 m/s case is 812 ± 5 μm, while the fragments sizes decrease and the distribution becomes wider for the 930 m/s case with values of 787 ± 7 μm. Note that this distribution only considers fragments larger than 10 μm, which corresponds to approximately 15 pixels in area in our optical microscope images. In addition to the inflection at 30 and 70 μm, the total number of fragments increases for increasing impact velocity, with a total of 22,000 fragments measured for the 275 m/s case and 28,000 total fragments measured for the 930 m/s velocity case. These represent some of the most complete fragmentation data sets in the literature. As discussed previously, the increase in the total number of fragments, especially the sub-30 μm population, is related to: (1) increased cracking to dissipate strain energy and (2) increased activation in the number of defects and subsequent coalescence of those fracture. We explore the possible reasons for the greater number of fragments for the various size ranges in the discussion once other aspects of the fragmentation processes are presented (e.g., shape, failure mechanisms).

Next, the normalized cumulative distribution of fragmentation aspect ratios is considered, presented and defined in Figure 3c. As the impact velocity is increased, the curve shifts to the right, indicating that there is an increase in the aspect ratio of fragments for increasing impact velocity (i.e., they become more shard-like). The non-normalized cumulative distribution of aspect ratios is plotted in Figure 3d, and this provides insights into the generation of *more* fragments for the higher velocity case. Namely, the distributions for the two impact velocities track each other reasonably well for aspect ratios less than 2.3. For both cases, this corresponds to approximately 20,000 total fragments. The two curves begin to deviate from each other for aspect ratios larger than 2.3, indicating the increased number of fragments for the higher velocity case is predominantly associated with the generation of more elongated fragments. It should be noted, however, that this is coupled with the occurrence of smaller fragments for the higher velocity case, and these elongated fragments occur across all size ranges (see Figure 2b).

3.2. Failure Mechanisms: Important Microstructure Features

The failure mechanisms leading to shard and blocky fragments are investigated further in SEM images in Figure 4. The two fragmentation types are highlighted in the optical image in Figure 4a with red and blue boxes (alluding to the original tile orientation), and include a schematic of the as-received tile showing the carbonaceous disk orientation and the direction of impact. Blue squares are used to denote planes that are close to normal to the hot-pressing direction, and red to denote planes that are close to parallel to the hot-pressing direction. First, a typical fracture surface of a blocky fragment is examined in Figure 4b. The SEM image shows larger elliptical graphitic defects protruding from the surface (indicated with arrows), and a crack spanning between them. This suggests that fracture is initiated from the disks, which is consistent with observations in uniaxial compression tests for the same material [15, 20]. Note here that these graphite defects appear to have the same orientation as those observed in the in-plane direction face (Figure 1b), where graphite disks appear as ellipsoids. In addition, the fracture surfaces are also relatively smooth, indicating transgranular fracture is dominant under impact conditions. This is consistent with uniaxial compression experiments [15, 20].

Next, fracture surfaces on a shard fragment is considered in Figure 4c and d. A lower magnification SEM image of an example of a shard fragment is shown in Figure 4c. Highlighted on the surface are larger carbonaceous defects (identified using Raman and EDS). A higher magnification image is shown in Figure 4d, again with the graphitic defects highlighted. These graphitic defects have different orientations than those on the blocky fragments. On the major axis of the shard surface, the graphite disks are oriented like those observed on faces normal to the hot-pressing direction (or impact direction). Essentially, these are oriented normal to the hot-pressing and impact direction. Combined, these results would indicate that the graphitic disks are primary sites for fracture initiation. The generation of blocky fragments results from the coalescence of fractures growing mostly parallel to the hot-pressing and impact direction. The major surface of shard fragments is linked to fractures growing perpendicular to the hot-pressing and impact direction.

Finally, potential evidence of amorphization on the fracture surface is explored for both the blocky and shard fragments using Raman Spectroscopy (Figure 5). Shown on the left in Figure 5a are representative Raman spectra from a blocky fragment (A,B in spectra plot) and shard fragment (C,D in spectra plot). In all spectra, the peaks associated with the boron carbide (B_4C), graphitic carbon, and boron nitride (h-BN) are denoted. For the tens of fragments examined for both blocky and shard fragments, similar features in the spectra are observed. Maps of individual phases are shown in Figure 5b and c on a blocky and shard fragment surface, respectively. Carbon defects (red in color), boron nitride (cyan), and amorphized (blue) phases are mapped onto the fracture surface. Based on the absence of high-frequency Raman bands characteristic of amorphous boron carbide [21], it can be inferred that stress-induced amorphization in boron carbide does not occur on the surface of any blocky and shard fragments studied in this investigation. Note that these fragments were typically larger than 100 microns in size. This may be somewhat expected as these fragments are likely generated away from the impact site, whereas amorphization typically occurs immediately beneath the projectile [21].

3.3. Linking Fragment Size and Microstructure Length Scales

In this final sub-section, inherent microstructural length scales are related to fragment sizes. Figure 6 shows the cumulative distribution of fragment sizes for the 930 m/s experiment (green curve to the right). Inflections in the fragment size distribution are present at 30 μm and 70 μm. Also shown in the figure is the cumulative distribution of: (1) graphitic disk spacing as observed on the shard fragment surface (blue curve and top left image), and (2) graphitic disk spacing in the in-plane direction (red curve and top right image). The distribution of graphitic disk spacing in the microstructure was previously published in Hogan et al. [15], while the image processing techniques developed by Hogan et al. [15] were used on images similar to those in Figure 4d to determine the graphitic disk spacing on the surface of shard fragments. For the defect spacing measurements, a total of 350 images were analyzed. A comparison of the disk spacing in the microstructure (red curve) and the fragment size distributions would suggest that the inflection at 70 μm appears to coincide with the spacing between the graphitic disks. A dashed line is extended from the off-set of the spacing distribution through the fragment size distribution for clarity. The comparison of the disk spacing on the shard surface (blue curve) and the fragment sizes suggest that the inflection at 30 μm appears to correspond with the spacings between the graphitic inclusions on the plane on the shard surface. Again, a line is extended through the off-set of the spacing distribution through the fragment size distribution to show that they closely coincide.

4. Discussion

Experimental results from the impact-induced fragmentation of a hot-pressed boron carbide indicate that two fragmentation mechanisms exist as a consequence of impact. These mechanisms can be classified based on their fragment size and relation to the defect spacing as follows:

- Mechanism 1: Few *larger* graphitic disk defects are activated due to nominally lower strain rates are sites which are away (in a relative sense) from the impact site. Fragmentation results would indicate that these defects are spaced relatively further apart as this mechanism generates fragments larger than 70 μm in size. Resulting fragment sizes are a consequence of the degree of the interaction and coalescence of radial, circumferential, and axial cracks, which are influenced by the structural deformation of the target. In this sense, this fragmentation is "structural-dominated". The fragment sizes in the mechanism appear to have a lower bound coinciding to that of the maximum spacing between defects (graphitic disks-70 μm), and, thus, one can affect fragment sizes in this regime by changing the defect spacing.
- Mechanism 2: All defects are activated locally due to high stresses and rates. This can happen, for example, as a consequence of abrasion and friction contact, an idea presented by Hogan et al. [16] based on previous work by Janach [22]. The

> distribution of defect sizes and their spacings are important in controlling fragmentation outcomes. In this sense, this fragmentation mechanism is "microstructural-controlled". In this hot-pressed boron carbide, this fragmentation mechanism creates fragments less than 30 μm in size and is associated with the coalescence of fractures originating from graphitic disks oriented more-or-less normal to the impact and hot-pressing direction.

Limited fragmentation exists between 30 and 70 μm for this hot-pressed material because of the two distinct fragmentation mechanisms. Similar mechanisms are reported for uniaxial compressive failure of this material, but the impact failure processes introduces additional interesting considerations regarding fragment shape (i.e., low aspect ratio blocky and high aspect ratio shard fragments). Within both fragmentation populations, shard and blocky fragments exist. The generation of more shard fragments was found to be mainly responsible for the increase in total number of fragments for increasing impact velocity, and also the increase in the sub-30 μm fragment population. This would indicate that there are more fractures normal to the impact direction for the higher velocity experiment, and this is a consequence of more fractures needed to dissipate its absorbed strain energy due to less relative time available for the material to deform structurally. Interestingly, a notable increase in the number of shard fragments in boron carbide was also observed by Moynihan et al. [7], which later motivated the research of impact-induced amorphization by Chen et al. [6]. In contrast to [6], there was no evidence of amorphization found on the shard fragments, or any other fragments, among those considered. Instead, brittle fracture was found to be dominant fragment-forming failure process for the shard fragments, and it was observed that the major axis of the shard fragments were aligned close to normal to the hot-pressing and impact direction.

We believe the notable production of shard fragments in this hot-pressed boron carbide materials is related to the shape and preferred orientation of the carbonaceous disks.

4.1. Implications

Results from this study have shown that fragment sizes and shapes derived as a consequence of impact are inherently related to defect orientations and spacings. By controlling the spacing between the defects, one can possibly control: (1) the fragment sizes in the microstructural-controlled fragmentation mechanism and (2) the lower bound of fragment sizes in the structural-controlled fragmentation mechanism. Increasing the graphite disk spacing (by reducing the number of defects) would thus increase the fragment sizes. According to recent work by Krell and Strassburger [1], larger fragments have been found to be correlated with improved ballistic performance of monolithic ceramic systems. This is a consequence of larger fragments interlocking better, thus providing improved projectile erosion. While independent impact tests are underway to verify the links between microstructure, fragmentation and performance, there exists an example in the open literature by Sano et al. [19] which illustrates relationships between microstructure and performance. This complements the links made in this paper between microstructure and fragmentation, and the links made by Krell and Strassburger [1] of fragmentation and performance. In the Sano et al. [19] study, ballistic performance curves for two boron carbide materials were presented (micrographs in Figure 7): (a) a pressureless sintered (PS) boron carbide and (b) a hot-pressed (PAD) boron carbide material similar to the one used in the current study. The materials have different defect populations (spacing and size), and nominally the same material properties (i.e., stiffness, dynamic strength, and hardness, as reported in [14]). It is noted that porosity plays a role in these results, and the differences is perhaps reflected in their densities: hot-pressed was 2,510 kg/m^3 and the pressureless sintered was 2,460 kg/m^3 [14]. Shown in Figure 7 is the corresponding ballistic performance results from the Sano et al. [19] study. In the ballistic curve sub-figure, the probability of tile penetration is plotted against a normalized velocity, which is not reported here. One can see from Figure 7 that the penetration resistance is much better for the hot-pressed material across all normalized velocities than the pressureless sintered material. Analysis of the microstructure would indicate that the PAD material has less defects and these defects are spaced further apart. The PAD material would likely have larger fragment sizes (according to our paper) and, thus, should have improved ballistic performance according to Krell and Strassburger [1]; it does according to these results. Altogether, the combination of results from the current paper, and the work by Krell and Strassburger [1] and by Sano et al. [19] provide motivation for continuing to study the link between microstructure, fragmentation, and ballistic performance.

5. Concluding Remarks

The impact-induced fragmentation of a hot-pressed boron carbide has been investigated, and inherent defect spacing length scales and orientations in directions normal and parallel to the hot-pressing direction were shown to strongly affect failure and fragmentation size and shapes. Altogether, the results presented in this paper demonstrate how a few well-quantified experiments, fragmentation size and shape measurements and well-characterized failure mechanisms can offer much insight into the impact failure of ceramics. In the future, significant advancements will be made in our understanding of these links through the continuing advancement of new diagnostics tools (e.g., flash X-ray [23]) and computational models explicitly capturing defects [24]. Ultimately, we hope that insights provided here can be used in designing the next generation of lightweight ceramics for ballistic protection applications.

6. Acknowledgment

This research was sponsored by the US Army Research Laboratory and was accomplished under Cooperative Agreement Number W911NF-12-2-0022 and W911NF-16-2-0079 . The views and conclusions contained in this document are those of the authors and should not be interpreted as representing the official policies, either expressed or implied, of the Army Research Laboratory or the U.S. Government. The U.S. Government is authorized to reproduce and distribute reprints for Government purposes notwithstanding any copyright notation herein. We acknowledge Dr. Brian Schuster of US Army Research Laboratory for access to the impact facility. Jim Campbell is also thanked for his review.

7. References

[1] A. Krell, E. Strassburger, Order of influences on the ballistic resistance of armor ceramics and single crystals, Materials Science and Engineering: A 597 (0) (2014) 422 – 430.

[2] R. Woodward, W. Gooch, Jr, R. O'Donnell, W. Perciballi, B. Baxter, S. Pattie, A study of fragmentation in the ballistic impact of ceramics, International Journal of Impact Engineering 15 (5) (1994) 605 – 618.

[3] J. McCauley, E. Strassburger, P. Patel, B. Paliwal, K. T. Ramesh, Experimental observations on dynamic response of selected transparent armor materials, Experimental Mechanics 53 (1) (2013) 3–29.

[4] D. Orphal, R. Franzen, A. Charters, T. Menna, A. Piekutowski, Penetration of confined boron carbide targets by tungsten long rods at impact velocities from 1.5 to 5.0 km/s, International Journal of Impact Engineering 19 (1) (1997) 15 – 29.

[5] J. LaSalvia, R. McCuiston, G. Fanchini, J. McCauley, M. Chhowalla, H. Miller, D. MacKenzie, Shear localization in a sphere-impacted armor-grade boron carbide, in: Proceedings of the 23rdInternational Symposium on Ballistics, 2007, pp. 1329–37.

[6] M. Chen, J. W. McCauley, K. J. Hemker, Shock-induced localized amorphization in boron carbide, Science 299 (5612) (2003) 1563–1566.

[7] T. Moynihan, J. LaSalvia, M. Burkins, Analysis of shatter gap phenomenon in a boron carbide/composite laminate armor system, in: 20th International Ballistics Symposium, v2 Terminal Ballistics, eds. J. Carleone and D. Orphal, DEStech Publications, Lancaster, Pennsylvania, 2002, pp. 1096–1103.

[8] J. Clayton, Mesoscale modeling of dynamic compression of boron carbide polycrystals, Mechanics Research Communications 49 (0) (2013) 57 – 64.

[9] D. Ge, V. Domnich, T. Juliano, E. Stach, Y. Gogotsi, Structural damage in boron carbide under contact loading, Acta Materialia 52 (13) (2004) 3921–3927.

[10] G. Fanchini, J. W. McCauley, M. Chhowalla, Behavior of disordered boron carbide under stress, Physical review letters 97 (3) (2006) 035502.

[11] D. Ghosh, G. Subhash, C. H. Lee, Y. K. Yap, Strain-induced formation of carbon and boron clusters in boron carbide during dynamic indentation, Applied Physics Letters 91 (6) (2007) 061910.

[12] X. Yan, Z. Tang, L. Zhang, J. Guo, C. Jin, Y. Zhang, T. Goto, J. McCauley, M. Chen, Depressurization amorphization of single-crystal boron carbide, Physical review letters 102 (7) (2009) 075505.

[13] D. E. Grady, Adiabatic shear failure in brittle solids, International Journal of Impact Engineering 38 (7) (2011) 661–667.

[14] J. D. Hogan, L. Farbaniec, T. Sano, M. Shaeffer, K. Ramesh, The effects of defects on the uniaxial compressive strength and failure of an advanced ceramic, Acta Materialia 102 (2016) 263–272.

[15] J. D. Hogan, L. Farbaniec, M. Shaeffer, K. Ramesh, The effects of microstructure and confinement on the compressive fragmentation of an advanced ceramic, Journal of the American Ceramic Society 98 (3) (2015) 902–912.

[16] J. D. Hogan, L. Farbaniec, N. Daphalapurkar, K. Ramesh, On compressive brittle fragmentation, Journal of the American Ceramic Society 99 (6) (2016) 2159–2169.

[17] A. Krell, E. Strassburger, T. Hutzler, J. Klimke, Single and polycrystalline transparent ceramic armor with different crystal structure, Journal of the American Ceramic Society 96 (9) (2013) 2718–2721.

[18] D. A. Shockey, D. R. Curran, L. Seaman, J. T. Rosenberg, C. F. Petersen, Fragmentation of rock under dynamic loads, International Journal of Rock Mechanics and Mining Sciences 11 (8) (1974) 303 – 317.

[19] T. Sano, M. Shaeffer, L. Vargas-Gonzalez, J. Pomerantz, High strain rate performance of pressureless sintered boron carbide, in: Dynamic Behavior of Materials, Volume 1, Springer, 2014, pp. 13–19.

[20] L. Farbaniec, J. Hogan, K. Ramesh, Micromechanisms associated with the dynamic compressive failure of hot-pressed boron carbide, Scripta Materialia 106 (2015) 52–56.

[21] V. Domnich, S. Reynaud, R. A. Haber, M. Chhowalla, Boron carbide: structure, properties, and stability under stress, Journal of the American Ceramic Society 94 (11) (2011) 3605–3628.

[22] W. Janach, The role of bulking in brittle failure of rocks under rapid compression, in: International Journal of Rock Mechanics and Mining Sciences & Geomechanics Abstracts, Vol. 13, Elsevier, 1976, pp. 177–186.

[23] B. E. Schuster, B. B. Aydelotte, R. B. Leavy, S. Satapathy, M. B. Zellner, Concurrent velocimetry and flash x-ray characterization of impact and penetration in an armor ceramic, Procedia Engineering 103 (2015) 553–560.

[24] A. L. Tonge, K. Ramesh, Multi-scale defect interactions in high-rate brittle material failure. part i: Model formulation and application to alon, Journal of the Mechanics and Physics of Solids 86 (2016) 117–149.

List of Figures

1 (top left) Schematic of boron carbide tile with hot-pressing direction labelled and conceptual graphite disk defects. Optical microscope images of boron carbide microstructure for (a) through-thickness direction and (b) in-plane direction. Labeled in these images are microstructural features (defined in top left of image (a)) and the impact direction of the spherical projectile (the dark circular object). 23

2 (a) Optical microscope image of ballistic fragments from an impact experiment at 930 m/s, and corresponding (b) scatter plot of aspect ratio vs fragment size. 24

3 (a) Normalized cumulative distribution of fragment sizes, (b) non-normalized cumulative distribution of fragment sizes, (c) normalized cumulative distribution of fragment aspect ratios (a/b), and (d) non-normalized cumulative distribution of fragment aspect ratios. 25

4 (a) Optical microscope image of fragments from 930 m/s experiment showing shard-like fragment (blue box) and blocky fragment (red box), and scanning electron microscope images of: (b) fracture surface of blocky fragment with graphitic disks labeled, (c) shard fragment with noticeable graphitic defects on the surface, and (d) magnified image of shard fracture surface with graphitic disks labeled. As a reference, the as-received tile with the hot-pressing and impact direction are labeled. Blue is used to denote images taken on planes more-or-less normal to the hot-pressing direction, and the red used to denote images taken on planes more-or-less parallel to the hot-pressing direction. 26

5 Impact velocity of 930 m/s: (a) Typical Raman spectra of the fracture surfaces in blocky (A, B in spectra plot) and shard (or elongated) (C, D in spectra plot) ballistic fragments. (b) Blocky fragment surface: the distributions of graphitic carbon inclusions (red) hexagonal boron nitride inclusions (cyan), and amorphized boron carbide (blue). (c) Shard fragment surface: the distributions of graphitic carbon inclusions (red) hexagonal boron nitride inclusions (cyan), and amorphized boron carbide (blue). The phase distribution maps were generated based on the intensities of the 1590 cm^{-1} line (graphite), 1367 scm^{-1} line (h-BN), and 1810 cm^{-1} line (amorphized boron carbide). The absence of blue colored regions in (b) and (c) indicates that no amorphization has occurred in boron carbide fracture surfaces under consideration in this study. . . 27
6 Cumulative distribution of fragment sizes (green curve) and (1) spacing between graphitic disks on the shard fragments (blue curve, image in top left) and (2) graphitic disk spacing in the in-plane direction (red curve, image in top right). We extend lines from the defect spacing distributions through the fragment size distributions to show that they are similar in value, suggesting a link may exist between fragment size and defect spacing. 28
7 SEM images of the pressure-less sintered and hot-pressed boron carbide microstructures with the corresponding figure of the probability of tile penetration plotted against a normalized velocity (not provided). Images and the plot are replicated from Sano et al. [19]. 29

List of Tables

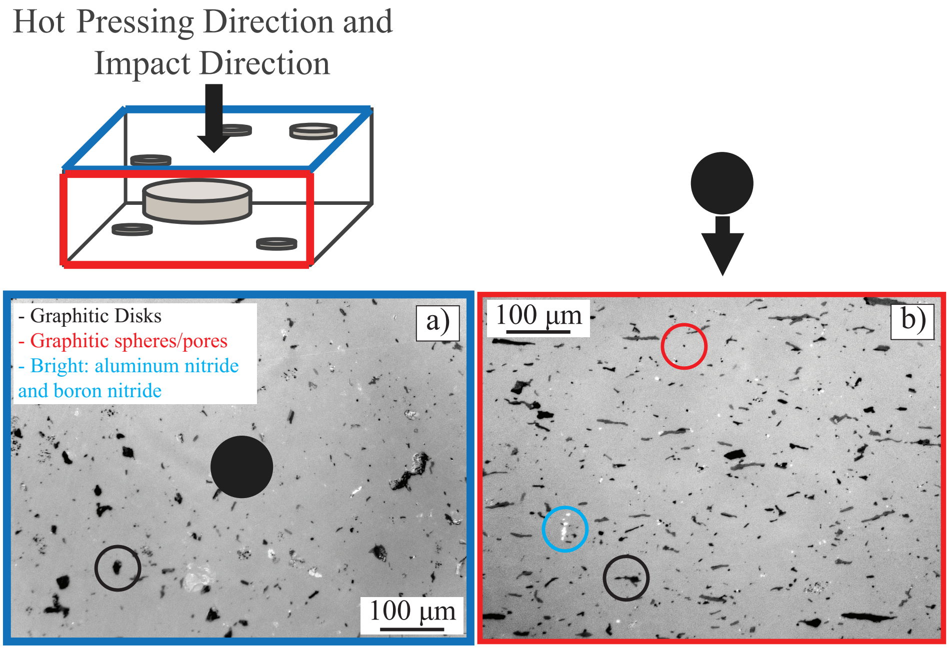

Fig. 1: (top left) Schematic of boron carbide tile with hot-pressing direction labelled and conceptual graphite disk defects. Optical microscope images of boron carbide microstructure for (a) through-thickness direction and (b) in-plane direction. Labeled in these images are microstructural features (defined in top left of image (a)) and the impact direction of the spherical projectile (the dark circular object).

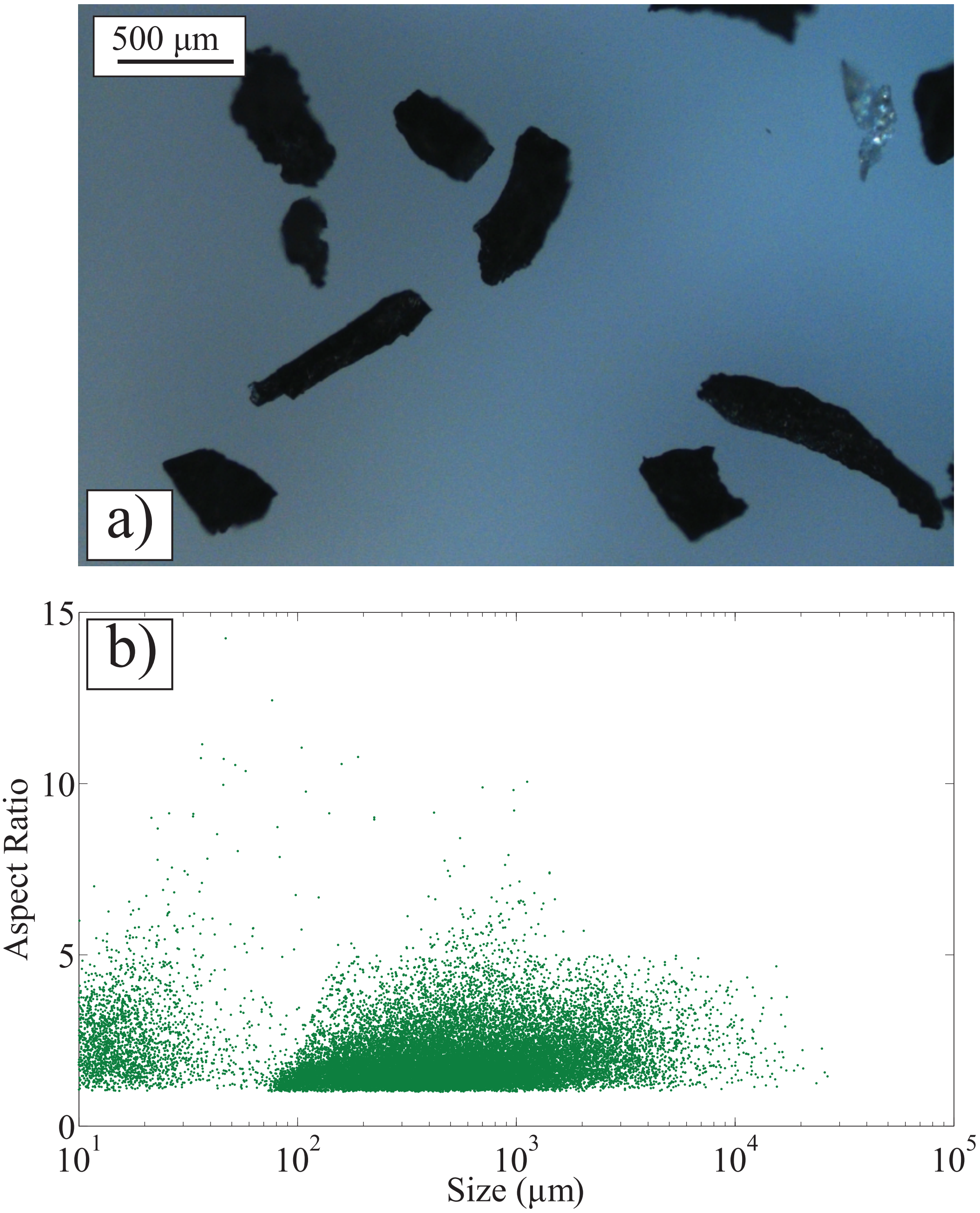

Fig. 2: (a) Optical microscope image of ballistic fragments from an impact experiment at 930 m/s, and corresponding (b) scatter plot of aspect ratio vs fragment size.

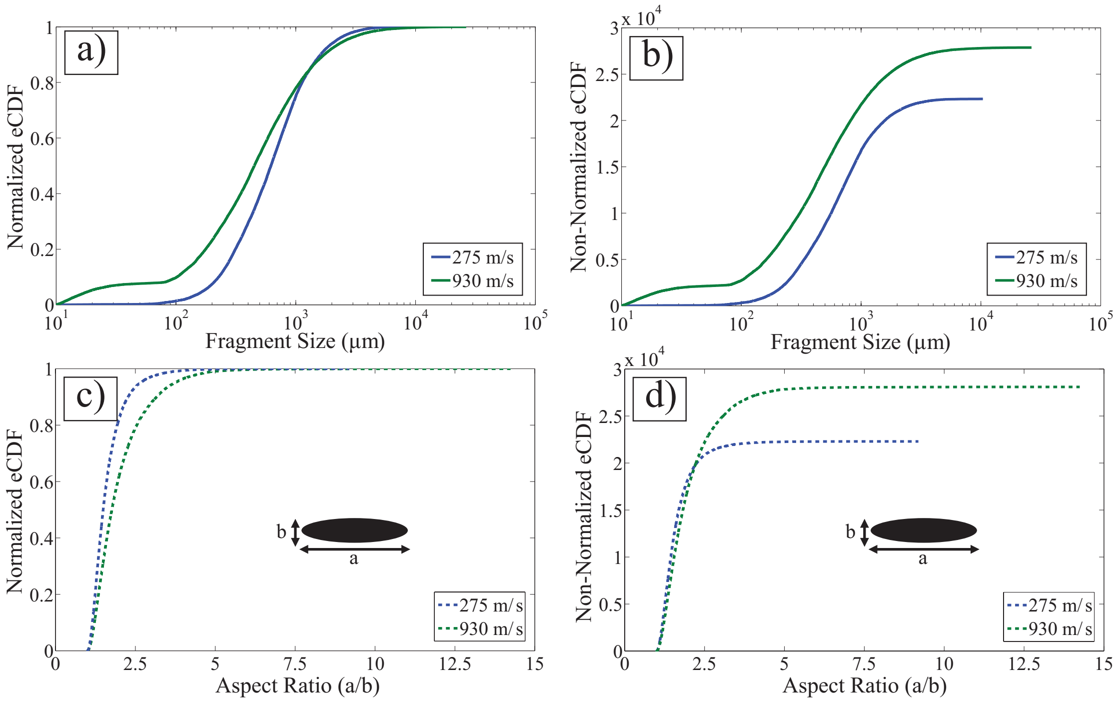

Fig. 3: (a) Normalized cumulative distribution of fragment sizes, (b) non-normalized cumulative distribution of fragment sizes, (c) normalized cumulative distribution of fragment aspect ratios (a/b), and (d) non-normalized cumulative distribution of fragment aspect ratios.

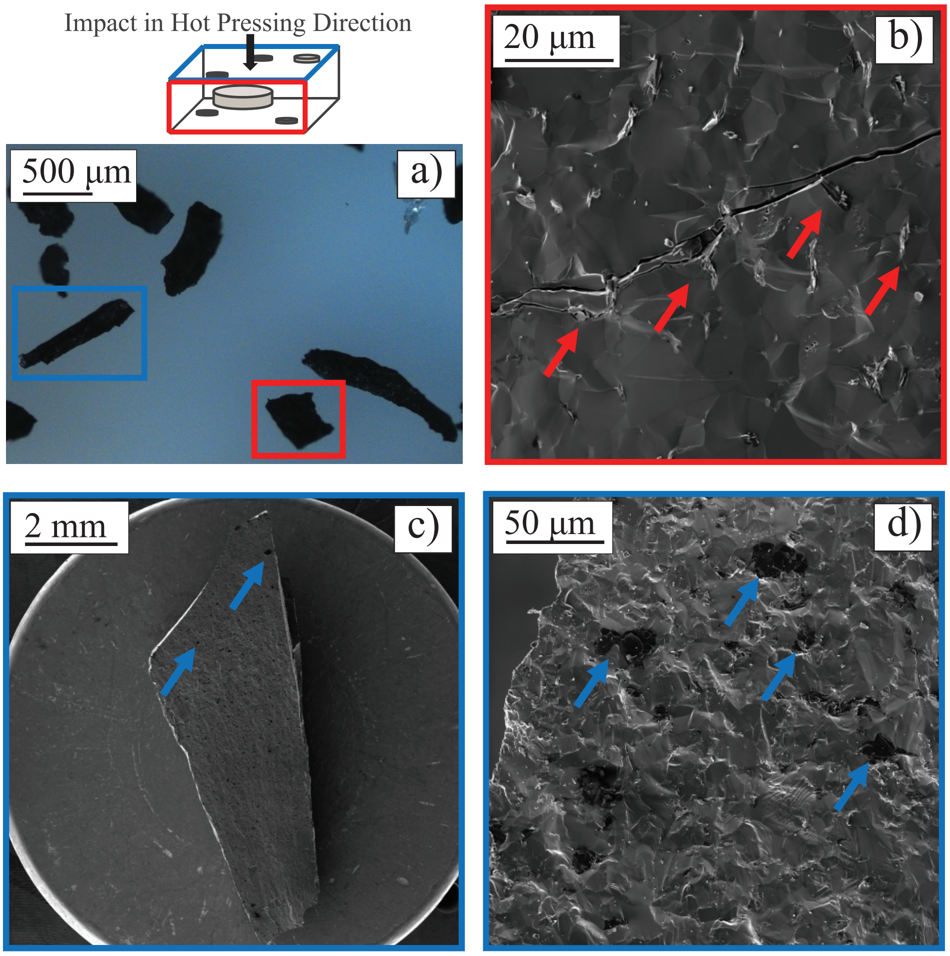

Fig. 4: (a) Optical microscope image of fragments from 930 m/s experiment showing shard-like fragment (blue box) and blocky fragment (red box), and scanning electron microscope images of: (b) fracture surface of blocky fragment with graphitic disks labeled, (c) shard fragment with noticeable graphitic defects on the surface, and (d) magnified image of shard fracture surface with graphitic disks labeled. As a reference, the as-received tile with the hot-pressing and impact direction are labeled. Blue is used to denote images taken on planes more-or-less normal to the hot-pressing direction, and the red used to denote images taken on planes more-or-less parallel to the hot-pressing direction.

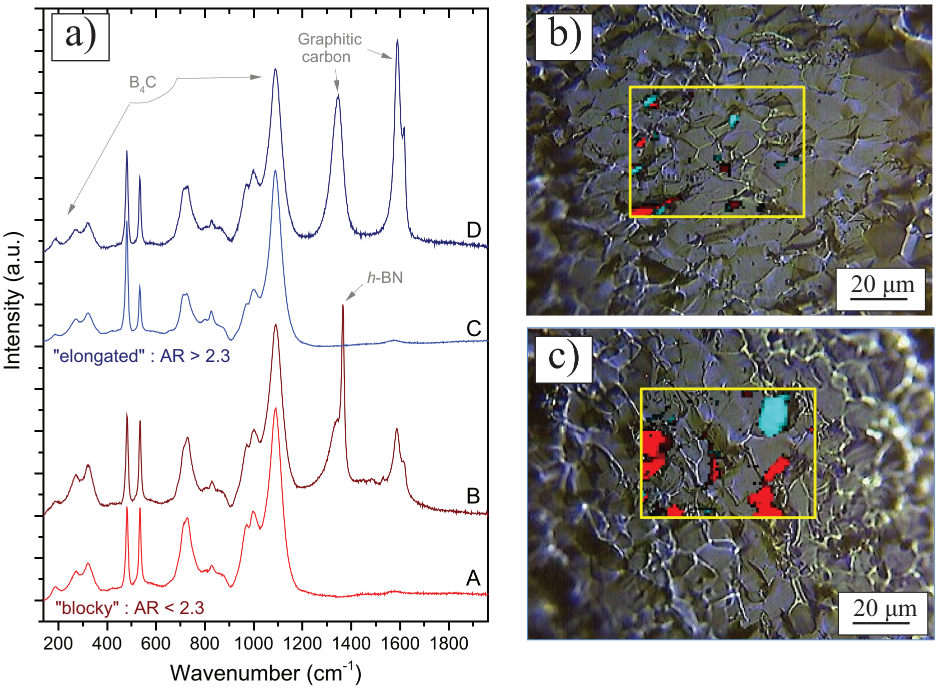

Fig. 5: Impact velocity of 930 m/s: (a) Typical Raman spectra of the fracture surfaces in blocky (A, B in spectra plot) and shard (or elongated) (C, D in spectra plot) ballistic fragments. (b) Blocky fragment surface: the distributions of graphitic carbon inclusions (red) hexagonal boron nitride inclusions (cyan), and amorphized boron carbide (blue). (c) Shard fragment surface: the distributions of graphitic carbon inclusions (red) hexagonal boron nitride inclusions (cyan), and amorphized boron carbide (blue). The phase distribution maps were generated based on the intensities of the 1590 cm^{-1} line (graphite), 1367 scm^{-1} line (h-BN), and 1810 cm^{-1} line (amorphized boron carbide). The absence of blue colored regions in (b) and (c) indicates that no amorphization has occurred in boron carbide fracture surfaces under consideration in this study.

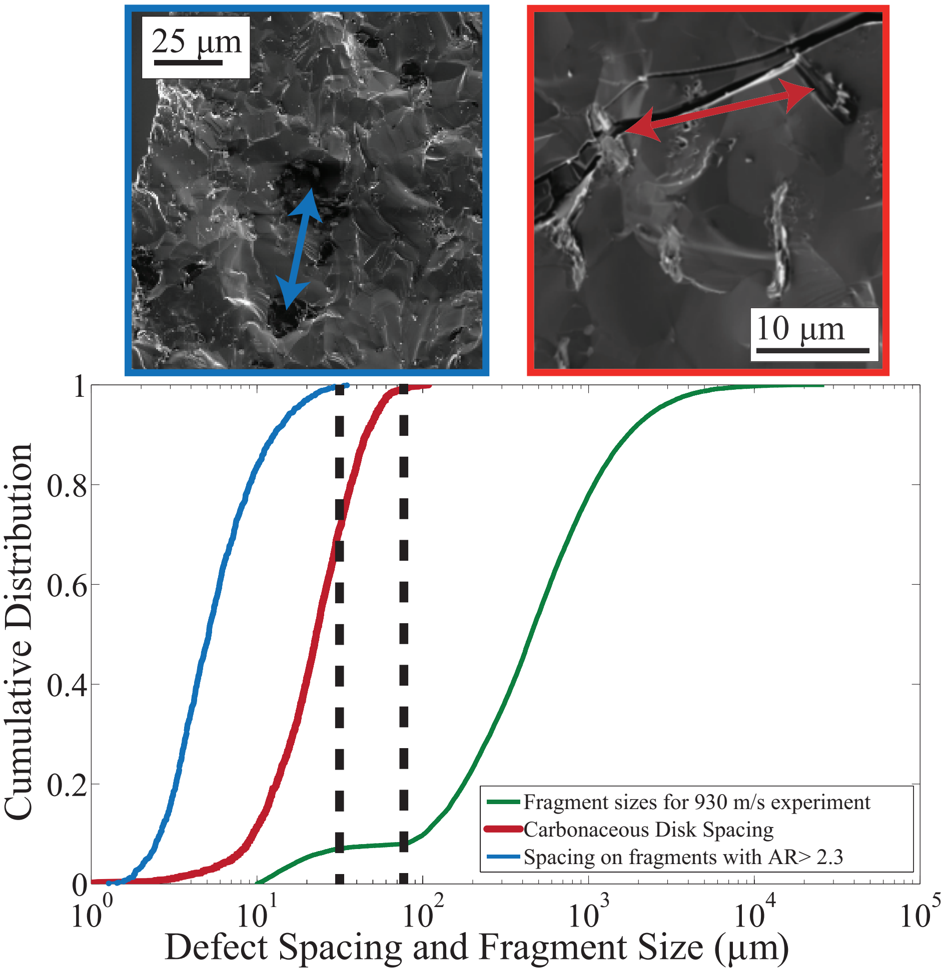

Fig. 6: Cumulative distribution of fragment sizes (green curve) and (1) spacing between graphitic disks on the shard fragments (blue curve, image in top left) and (2) graphitic disk spacing in the in-plane direction (red curve, image in top right). We extend lines from the defect spacing distributions through the fragment size distributions to show that they are similar in value, suggesting a link may exist between fragment size and defect spacing.

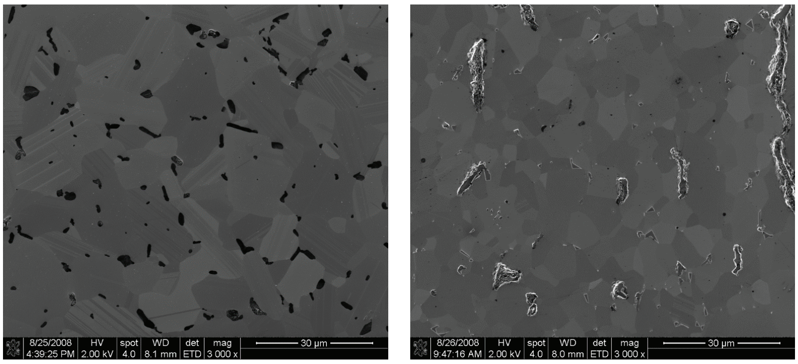

Pressure-less sintered (PS) Hot-pressed (PAD B4C)

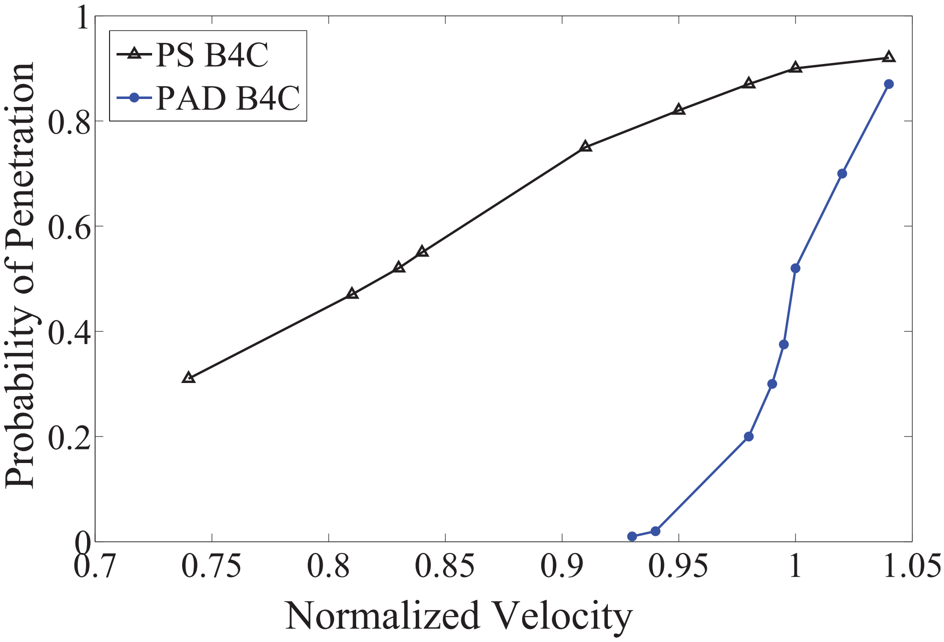

Fig. 7: SEM images of the pressure-less sintered and hot-pressed boron carbide microstructures with the corresponding figure of the probability of tile penetration plotted against a normalized velocity (not provided). Images and the plot are replicated from Sano et al. [19].

Highlights:

The impact failure and fragmentation of boron carbide is studied experimentally.

Key microstructure defects are identified, quantified, and then linked with fragmentation size and shape measurements.

The results provide motivation for tailoring defect populations in order to control fragmentation and performance.